RESEARCH ARTICLE

Effect of La Dopant in Modified Bismuth Ferrite Ceramics

R.K. Parida[1], B.N Parida[2], R. K. Bhuyan[3] and S. K. Parida[1,]*

The La modified bismuth ferrite perovskite $Bi_{0.6}La_{0.4}FeO_3$ (BLF) is prepared by cost-effective high solid-solution casting technique. Formation of composite is checked through X-ray diffraction and also notable that there is phase transition from rhombohedral (R3c) to orthorhombic (Pbnm). The average crystalline size (D_{SC}) and mechanical lattice strain are 63.8 nm and 0.147% respectively as calculated by Williamson-Hall method. The frequency bands corresponding to Bi-O, LaO, and FeO stretching vibration confirm that La^{+3} ions completely incorporate the Bi^{+3} ions in the A-site of the single perovskite. The SEM micrograph suggests that the sample has distinct grains and well-defined grain boundaries and the average grain size (D_{SEM}) is about 13.9 µm. The rate of agglomeration that acquire in the sample (D_{SEM}/ D_{SC} = 219) confirms the excellent connectivity of grains which stands possible reason for the high dielectric and conductivity. The impedance analysis provided the fact that bulk resistance (R_b) decreases from 6.662 x 10^5 Ω at 25^0C to 1.000 x 10^{-2} Ω at 350^0C; suggesting NTCR behaviour of the material. The activation energy increases from 201 meV to 677meV with temperature supports a thermally activated conduction mechanism. The thermally activated relaxation process is controlled by the immobile charge carriers at lower temperature range while controlled by defects at higher temperatures which suggests the presence of hopping mechanism. The gap between the peak of $Z''$and M'' is becoming wide with temperature suggests a non-Debye type character. The semicircular arcs in both Nyquist plots and Cole-Cole plots are confirming the semiconductor nature.

Introduction

Bismuth ferrite (BFO) ceramics with the addition of dopants exhibit exceptional electromechanical properties in either bulk or thin film form for various potential applications [**1,2**]. Out of all multiferroic materials, BFO has paid more attention due to the presence of magnetic orders (ferromagnetic or antiferromagnetic) and strong ferroelectric properties at room temperature. Moreover, BFO is a multiferroic material which has both ferroelectric and magnetic orders at above room temperature [**3,4**]. Thus, it has made an important impact on multiferroic nanomaterials area of research. The BFO-based nanomaterials in different forms were prepared, including BFO ceramics, thin films, and nanostructures are reports in the literature [**5-7**]. The Pierre Curie proposed in 1894 possibility of magnetoelectric (ME) effect in BFO thereafter a huge gap of research interest in said material. Around 1959, several research groups start working on this multiferroic material, but the first observation on the ME effect provides a lot of excitement because of the coupling between the electric and magnetic field in the matter produce various technological applications [**8,9**]. A detail of a decade of intense theoretical and experimental research on the electrodynamics of ME effect was summarized by O'Dell [**9**]. In the process of adding a dopant to the BFO materials, it has been noticed that there is a change in both densification and microstructure development during sintering. After substitution of La^{+3} in the Bi^{+3} site of the BFO, a change in magnetic properties of BFO was observed. It shows the coexistence of electric and magnetic properties i.e., ferroelectric ordering (T_c = 830^0 C) and anti-ferromagnetic ordering (T_n = 370^0 C). It has a rhombohedral, distorted perovskite structure with space group R3c at 300K [**10-13**]. Chunlin Fu *et. al.*, [**14**] studied structural and magnetic properties of bismuth ferrite nanopowders prepared via the Sol-Gel method and report that the electrical and magnetic properties of the doped materials enhanced. The study of the conducting thin layer of bismuth ferrite gives the enhanced magnetic properties

[1]Department of Physics, ITER, Siksha 'O' Anusandhan Deemed to be University, Bhubaneswar, India
[2]Department of Physics, Central Institute of Technology Kokrajhar, (Deemed to be university, MHRD, Govt. of India) BTAD, Assam 783370, India
[3]Government (Auto) College Angul, Angul 759143, India

*Corresponding author:
E-mail: santoshparida@soa.ac.in

DOI: 10.5185/amlett.2021.081656

nearly 15 times compared to the corresponding bulk sample [**15,16**].

The study of the structural, dielectric, conductivity, optical, magnetic behaviour of doped BFO ceramics is reported in the literature [**17,18**], but doping with additive La ($x \leq 0.4$) in bismuth ferrite is scared. The additive in the given matrix is responsible to enhance the physical and chemical properties of the newly developed material. So, the synthesis $Bi_{0.5}La_{0.5}FeO_3$ single perovskite was planned. The structural and electrical properties of the sample were characterized by XRD, SEM, FTIR and LCR measurement. The findings of the paper are phase transition from rhombohedral to orthorhombic, D_{SEM}/D_{SC} = 219, thermally activated conductivity and semiconductor nature of the sample.

Experiment

The metal oxides such as Bi_2O_3 (99.0%), La_2O_3 (99.9%), and Fe_2O_3 (99.9%) are weighted stoichiometry amounts accurately up to the third decimal place using the digital spring balance. These metal oxides were thoroughly mixed by dry grinding method with the help of mortar pestle. For a better homogeneity mixture of the elements, a wet grinding method with methanol is adopted. A high-temperature silica crucible containing the powder sample is placed inside the high-temperature furnace at 1250^0C to fuse into one compound. Then, the $Bi_{0.6}La_{0.4}FeO_3$ single perovskite is prepared by high sintering method. After the calcination but before the sintering, the powdered sample was regrinding and pelletization was done under the pressure of 3 - 4 MPa at room temperature. The size of the prepared pellets is of discs 1 mm thick and 10 mm in diameter covered with silver electrodes. The formation of desired sample structure was confirmed by XRD (RIGAKU, Japan ULTIMA IV, Cu-K_α radiation; 1.5405 Å) profile and tolerance factor. The X'Pert-High Score Plus software is used to analysis structure and for the refine parameters Rietveld analysis was done. SEM micrograph is used to identify the distribution of the grains and grain boundaries using a JEOL 6360A Analytical Scanning Electron Microscope. The LCR meter (N4L PSM, 1735) is being used to calibrate electrical parameters from temperature 25^0C to 350^0C and frequency 1 kHz to 1 MHz.

Results and discussion

Structure formation

The general formulation of a perovskite is ABO_3, where A- and B- sites are replaced by divalent and tetravalent elements respectively. The tolerance factor of a perovskite material can be written as; $t = \frac{r_A + r_o}{\sqrt{2}(r_B + r_0)}$, where r_A = ionic radius of A-atom, r_B = ionic radius of B-atom and r_0 = ionic radius of oxygen-atom. In most of the cases, the conventional tolerance factor value should lie within the range from 0.75 to 1.0 with additional condition; $r_A > 0.9$ Å and $r_B > 0.51$ Å nm [**19**]. Robert Ian Hines reported a method to evaluate crystal structure by using tolerance factor value, where the possible value of t for different crystal structure are given like hexagonal crystal structure; $1.00 < t < 1.13$, for cubic structure; $0.9 < t < 1.0$, for orthorhombic structure $0.75 < t < 0.9$ and for $t < 0.75$, the structure was adopted to hexagonal ilmenite structure (FeTiO3) [**20**].The ionic radii of Bi^{3+}, La^{3+} and Fe^{+3} are 1.03 Å, 1.06 Å and 0.645 Å respectively [**21**]. For calculation, $r_A = Bi_{0.6}La_{0.4} = 0.6(1.03) + 0.4(1.06) = 1.042$Å, $r_B = 0.645$ Å and $r_0 = 1.4$ Å. Now, the value of the tolerance factor; $= \frac{r_A + r_o}{\sqrt{2}(r_B + r_0)} = \frac{1.042 + 1.4}{1.414(0.645 + 1.4)} = 0.84$. Therefore, La doped bismuth ferrite single perovskite has orthorhombic crystal.

XRD analysis and crystal strain calculation

The X-ray diffraction is an important tool to evaluate unknown phase, identification structure, space group, unit cell volume and density etc. **Fig. 1(a)** shows the XRD profile of the $Bi_{0.6}La_{0.4}FeO_3$ single perovskite. The XRD pattern suggests single phase formation due to the presence sharp and distinct intense peaks.

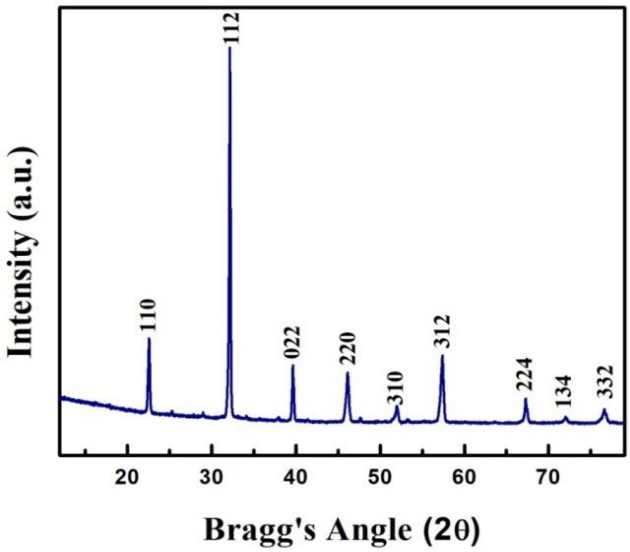

Fig. 1(a). XRD profile of the $Bi_{0.6}La_{0.4}FeO_3$ single perovskite.

XRD data is analysed by the PANALYTICAL X' PERT PRO MPD powder diffractometer with CuK_α radiation (λ = 0.15405 nm) and results suggest an orthorhombic crystal structure with space group Pbnm (JCPDS file No. 01-087-0108). **Fig. 1(b)** shows the Rietveld refinement of XRD data of the $Bi_{0.5}La_{0.5}FeO_3$ single perovskite using Pseudo-Voigt function [**22**]. The MAUD software is used to complete the rietveld refinement analysis of the experimental XRD data [**23**]. The refinement parameters of the sample are calculated with the simulation of different physical quantities including atomic position, the lattice constant, full width half maximum, shape parameter, scale factor and crystal orientation [**24**].

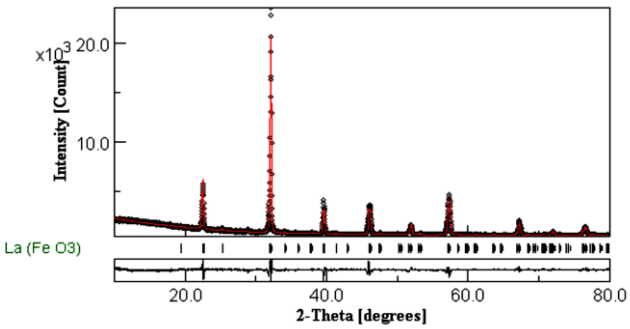

Fig. 1(b). Rietveld refinement of the $Bi_{0.6}La_{0.4}FeO_3$ single perovskite.

The refined cell parameters are given; a = 5.557Å, b = 5.565Å, c = 7.8543Å, α = 90⁰, β = 90⁰, γ = 90⁰, ρ = 6.64 g/cm³ and V = 262.2 Å³[ICSD code- 078064]. The reliability factors obtained from the Rietveld refinement are $R_{wp}(\%) = 7.29$, $R_{exp}(\%) = 3.20$, $R_B(\%) = 5.29$ and $GOF = (chi)^2 = 2.27$ are well-matched with the previously reported doped BFO compound [**25**]. The quality of the Rietveld refinement is excellent because of the most zero difference between experimental and computed data recorded. The crystal structure of the pure host matrix $BiFeO_3$is rhombohedral with space groupR3c, lattice constant 3.965 Å and a rhombohedral angle α = 89.3⁰ to 89.4⁰ at room temperature [**26-28**]. Therefore, there is a phase transition occurs from rhombohedral (R3c) to orthorhombic (Pbnm) after doping of La into the pure host BFO matrix. The presence of the crystal imperfection, dislocation, and defect in the sample gives peak broadening, crystalline size, and lattice strain. The crystallite size of sample can be determined by using the Scherer equation: $D = \frac{0.89\,\lambda}{\beta cos\theta}$, where λ = wavelength of the used light source (λ = 1.54056 Å), θ is the position of the diffraction peaks and β= full width half maximum measured in radians [**29**]. A plot is drawn taking $\frac{1}{\beta}$ along the *x*-axis and $cos\theta$ along the *y*-axis as shown in **Fig. 2(a)**. A linear fit line to the experimental data provides the average particle size, which is about 63.8 nm [**30**].

When La enters into the pure BFO host matrix, a lattice strain is produced in the prepared sample. The relation of the strain with the diffraction angle and FWHM is stated as $\varepsilon \approx \beta/tan\theta$. Therefore, this new method of calculation of strain is called the Williamson-Hall (W-H) method, in which strain (ε) varies with $tan\theta$. The net broadening of the peaks is calculated in the W-H method of calculation of the strain. They assumed the total broadening in a breath of Bragg's peak is the sum of the broadening due to crystallite size and strain. The distinct role of the θ induced size and strain broadening and can be evaluated by using the W-H method. Therefore,

$$\beta = \beta_{size} + \beta_{strain}$$
$$\Rightarrow \beta = \frac{k\lambda}{Dcos\theta} + 4\varepsilon tan\theta$$
$$\Rightarrow \beta cos\theta = \frac{k\lambda}{D} + 4\varepsilon sin\theta$$

The above equation is true only when the material is isotropic nature; it means the material properties are independent of the direction along which they are measured. The model is developed using the concept that the strain assumed to be uniform in all crystallographic directions called the Uniform Deformation model (UDM). Under the UDM calculation; the term $4sin\theta$ is plotted along the *x*-axis and $\beta cos\theta$ is plotted along the y-axis shown in **Fig. 2(b)**. The slope and *y*-intercept of the fitted line provides the strain and average crystalline size. The average crystalline size of the sample is about 65.7 nm calculated from the W-H method. During the formation of the sample, La atoms enter into the bismuth ferrite host matrix. So, there will be a bond stretching among different atoms inside the sample. Due to strong interaction and bond stretching in the sample, a mechanical strain is produced and can be calculated using the W-H relation, $\beta cos\theta = \frac{k\lambda}{D} + 4\varepsilon sin\theta$,where ε is the strain produced in sample. The mechanical strain that produces in the sample is about 0.147% [**31**].

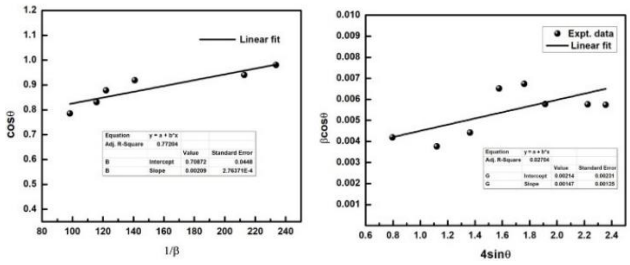

Fig. 2. (a) Scherer plots (b) Williamson-Hall plots of the $Bi_{0.6}La_{0.4}FeO_3$ single perovskite.

FTIR and SEM analysis

Fig. 3(a) represents the FTIR spectrum **Fig. 3(b)** SEM micrograph of the $Bi_{0.6}La_{0.4}FeO_3$ single perovskite. There are many absorption bands present in the mentioned wavenumber range 348-4700 cm^{-1}. There are different modes of vibrations observed at 385, 459, 532, 580, 1560, 1639, 2933, and 3445 cm^{-1}. The peaks are the response of the atoms that present in the material under study. In this mentioned wavenumber range, the formation of the peaks may be related to the unequal stretching relaxation of the B–O bond of trigonal BO_3 units [**32,33**]. The frequency bands corresponding to Bi-O, LaO, and FeO stretching vibration confirm that the La^{+3} ions completely incorporate the Bi^{+3} ions in the A-site of the single perovskite. SEM micrograph analysis indicates that sample has high density and minimum porosity because the grains are very closely packed. The grains are uniformly distributed through well-defined grain boundaries over the sample surface. This implies that the charge carriers due to Bi^{+3} or evaporation of the La^{+3} may be the reason of the leakage current. SEM intercept method is used to calculate the average grain size,

which is about 13.9µm. Here, the presence of small size grains protects dopant growth in the sample and leads to the larger surface area, which is require for upgrading the performance in application. The rate of agglomeration that acquire in the sample (D_{SEM}/ D_{SC} = 219) confirms the excellent connectivity of grains which stands possible reason for the elevated value of dielectric and conductivity [**34**].

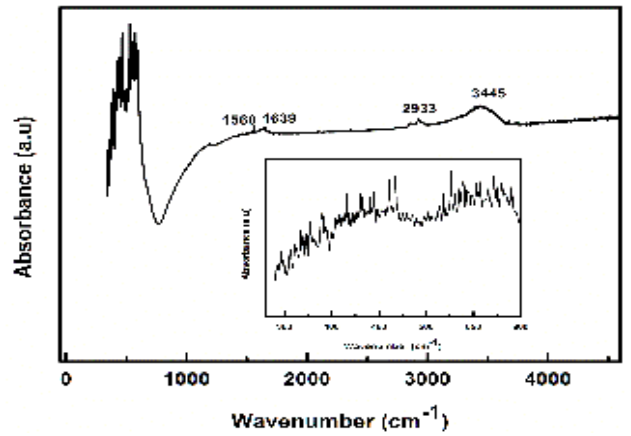

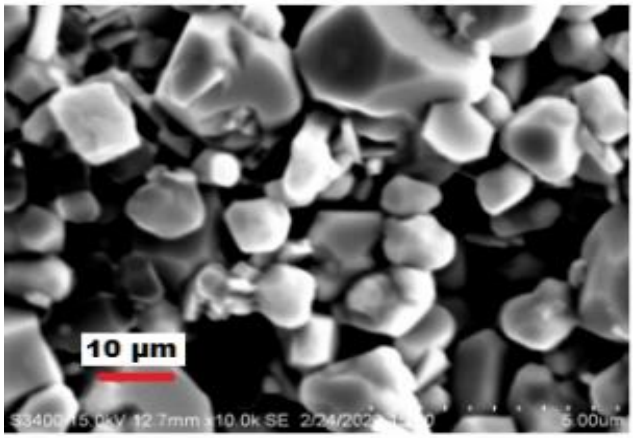

Fig. 3. (a) FTIR spectrum and (b) SEM micrograph of the $Bi_{0.6}La_{0.4}FeO_3$ single perovskite.

Modulus analysis

The discussion on the electrical modulus gives an idea about polarization vector, electric relaxation time, electrode effect, and most importantly electrical conductivity of materials under study. So, we need to study electrical modulus with a different frequency range. The expression of the real component of modulus (M') and imaginary components (M″) is mentioned as $M' = A\left\{\frac{(\omega RC)^2}{1+(\omega RC)^2}\right\}$ and $M'' = A\left\{\frac{\omega RC}{1+(\omega RC)^2}\right\}$, where $A = \frac{C_0}{C}$

Fig. 4(a) represents a graph between M′ versus frequency from temperature 25^{0}C to 350^{0}C. It is observed from the figure that the value of M′ is hailing zero in the low frequency and then continuous increase of M′ with rise of the frequency suggests to saturate maximum asymptotic value for each temperature. The saturated M′ value helps the short-range charge carriers in conduction mechanism [**35**]. The given interpretation is directly related to the absence of restoring force that guides the thermal activated charge carriers under the action of the electric field. But, the low value of M′ helps to the long-range mobility of charge carriers in the conduction mechanism [**36**]. **Fig. 4(b)** shows a graph between M″ versus frequency from 25^{0}C to 350^{0}C. The M″ increases with the rise of the frequency but it attains maximum and then decreases. The M''_{max} peaks are switched towards the high temperature and frequency region. The frequency below the M''_{max} provides a region for long range mobility of charge carriers whereas at the frequency above the M''_{max} provides a region for short range charge carriers that confined to potential well. However, the frequency at M''_{max} becomes the indicator of the conversion from long range to short range. This implies that there is a temperature dependent hopping process for conduction mechanism. The existence broaden peaks suggests a wide range of relaxation process depending on relaxation time constant [**37,38**]. Therefore, it may be concluded that, the shifting of the M''_{max} peaks with rise of temperature confirms a thermally activated relaxation process and presence of asymmetrical modulus plots proof the non-Debye type behaviour [**39**].

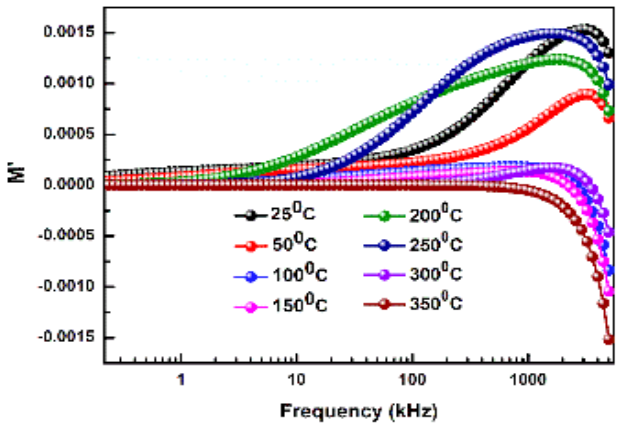

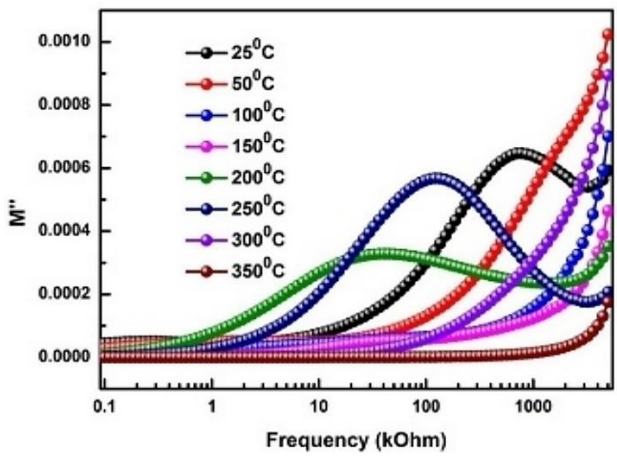

Fig. 4. (a) Variation of M′ vs. Frequency and (b) Variation of M″ vs. Frequency of the $Bi_{0.6}La_{0.4}FeO_3$ single perovskite.

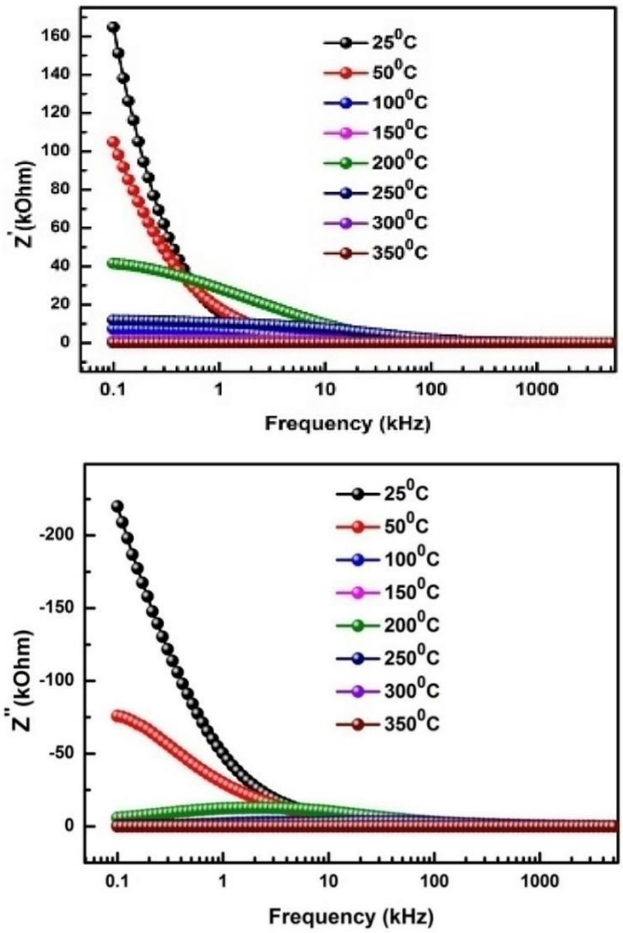

Fig. 5. (a) Variation of Z′ vs. Frequency and (b) Variation of Z″ vs. Frequency of the $Bi_{0.6}La_{0.4}FeO_3$ single perovskite.

Impedance analysis

Fig. 5(a) & **Fig. 5(b)** represent variation of Z′ and Z″ with frequency in wide range of temperature. The decreasing tendency of both Z′ and Z″ with rise of frequency and temperature suggest NTCR behavior i.e., semiconducting nature. All the value of Z′ and Z″ are combined into one at higher frequency and temperature suggesting the release of space charge, which decreases the barrier properties [**40**]. The existence of relaxation process at low-temperature region is due to electron mobility charge carriers at the same time oxygen vacancies or defects are responsible at high temperature. So, conduction mechanism is controlled by the hopping of the electrons, oxygen ion vacancies, and defects in the sample [**41**].

In **Fig. 6(a)** at fixed temperature 100^{0}C, the frequency dependence of the Z′ and Z″ of the $Bi_{0.6}La_{0.4}FeO_3$ single perovskite is reported. From the figure, it is observed that essence of two curves indicates the relaxation frequencies of Z′ and Z″ are compensating to each other. This nature of the curves suggests a non-Debye type of conductivity mechanism [**42**]. The relaxation time is calculated using the standard formula $\tau = \frac{1}{2\pi f_r}$, where f_r is called relaxation frequency. Activation energies of the sample are calculated by using Arrhenius model by plotting $ln(\tau)$ along y-axis and 1000/T (C^{-1}) along x-axis as shown in **Fig. 6(b)** [**43**]. The $Bi_{0.6}La_{0.4}FeO_3$ single perovskite has two activation energies; at higher temperature in between (100 – 350^{0}C), the activation energy of the sample is $E_{a2} = 1456$ meV and at low temperature (25 – 50^{0}C) is $E_{a1} = 897$ meV. It may be concluded that the existence of relaxation process in the sample may be managed by the immobile charge carriers at low-temperature at the same time defects at higher temperature [**44**].

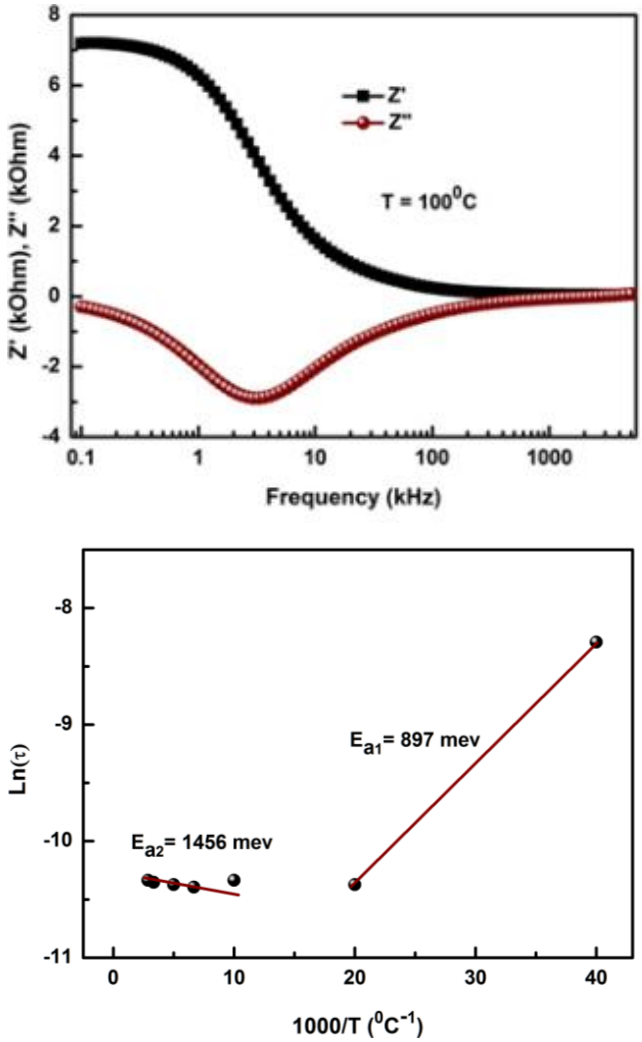

Fig. 6. (a) variation of Z′ and Z″ with frequency (b) variation of $ln(\tau)$ with temperature of the $Bi_{0.6}La_{0.4}FeO_3$ single perovskite.

At T = 200^{0}C in **Fig. 7(a)**, the two curves reveal a single peak at the same frequency, which confirm the domination of long-range movement of charge carriers [**45**]. At T = 250^{0}C in **Fig. 7(b)**, it is observed that the gap between the peak of Z″ and M″ is becoming wide with temperature, which enunciates the non-Debye-type relaxation behavior in the sample [**46,47**].

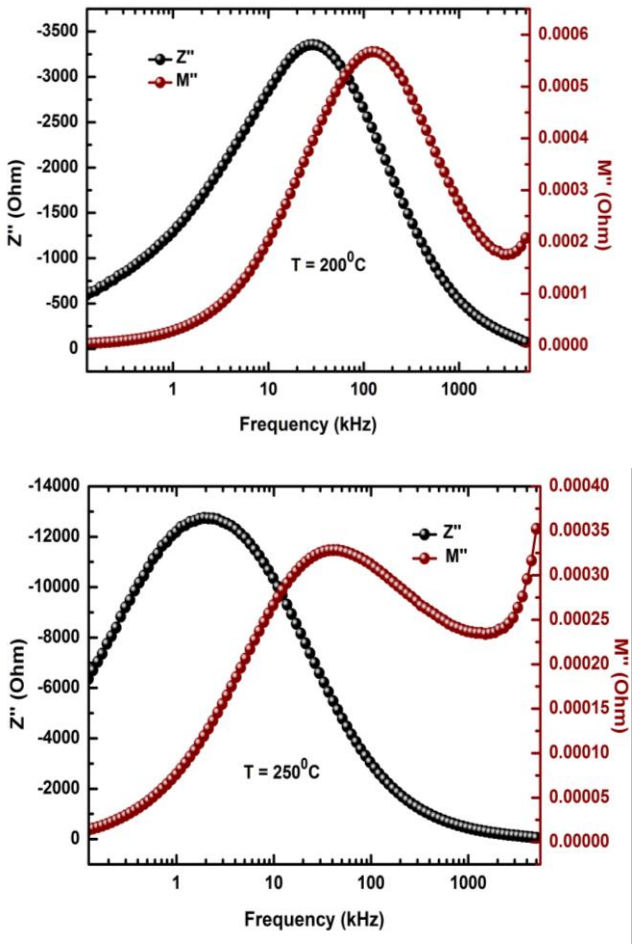

Fig. 7. (a) Combined plots imaginary part of impedance $Z''$and imaginary part of modulus M''versus frequency at 200^{0}C and (b) Combined plots imaginary part of impedance $Z''$and imaginary part of modulus M''versus frequency at 250^{0}C.

Nyquist and Cole-Cole Plot

To understand the conduction mechanism due to the effect of grain and grain boundaries in the prepared sample, **Fig. 8(a)** and **Fig. 8(b)** are presented. The software ZSIMPWIN version 2.0 was used to fit the Z' and Z''experimental data. The fitted curves are well matched with electrical circuit model LR(QR)(CR). It is calculated from fitting data that the bulk resistance (R_b) decreases from 6.662 x 10^5 Ω at 25^{0}C to 1.000 x 10^{-2} Ω at 350^{0}C; suggesting NTCR behaviour of the material. Similarly, the inductive resistance (R_L) also increases from 3.462 x 10^2 Ω /cm^2 to 1.000 x10^{-2} Ω /cm^2 during the variation of temperature from at 25^{0}C to 350^{0}C. The frequency power increases from 0.4 at 25^{0}C to 8.97 at 350^{0}C as mentioned in **Table 1**. It is observed that Nyquist plots are semicircular. The larger semicircles at low frequencies are due to the effect of grain boundaries while smaller semicircles at higher frequencies are due to the effect of bulk grains [**48**]. The Nyquist plots are semicircular, which supports the semiconducting nature of the sample [**49**].

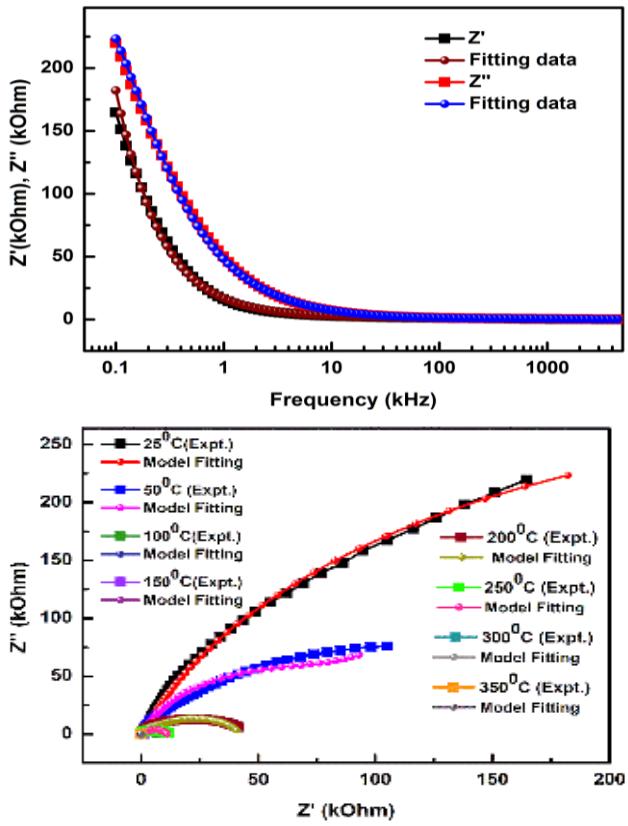

Fig. 8. (a) Shows variation of fitted data of Z′ and Z′′ with frequency at 200^{0}C and (b) represents fitting Nyquist plots of the $Bi_{0.6}La_{0.4}FeO_3$ single perovskite.

Fig. 9 shows the Cole-Cole plots of $Bi_{0.6}La_{0.4}FeO_3$ single perovskite. Normally, Cole–Cole plot is simulated with an equilibrium circuit element containing of resistance (R), capacitance (C), and sometimes inductance (L), in which the electrode interphase inherently incorporated structure. Therefore, real and imaginary part impedance plot may provide the state of electrode surface and also the kinetic of the metal electrode. The presence of prefect semicircular arcs of Cole-Cole plot demands semiconductor nature of the sample [**50**]. The above calculated electrical parameters are suitable for application in the energy storage devices.

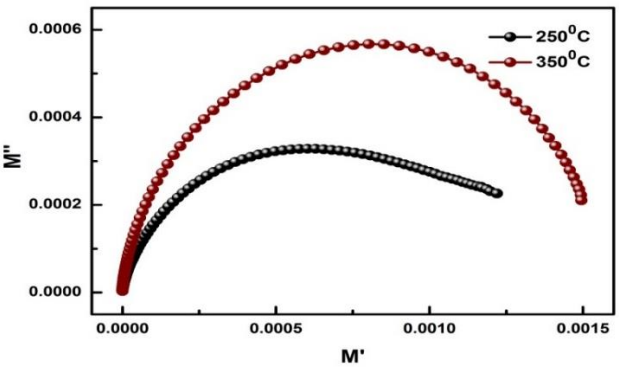

Fig. 9. Represents Cole-Cole plots of the $Bi_{0.6}La_{0.4}FeO_3$ single perovskite.

Table 1. List of the fitted data of equivalent circuit LR(QR)(CR): bulk inductance (L_b), Inductive resistance (R_L), constant phase factor (Q), bulk resistance (R_b), boundary resistance-capacitance (C_{gb}), grain boundary resistance (R_{gb}) and frequency power at 25^{0}C, 50^{0}C, 100^{0}C, 150^{0}C, 200^{0}C, 250^{0}C, 300^{0}C and 350^{0}C.

Temp.	L_b (H/cm^2)	R_L (Ω /cm^2)	Q (S-sec^5/cm^2)	R_b (Ω-cm^2)	C_{gb} (F/cm^2)	R_{gb} (Ω-cm^2)	Frequency power (n)
25^{0}C	4.649 x 10^{-17} (Expt.)	3.462 x 10^2 (Expt.)	1.234 x 10^{-8} (Expt.)	6.662 x 10^5 (Expt.)	4.213 x 10^{-10} (Expt.)	8.221 x 10^2 (Expt.)	
	9.961 x 10^{-19}(fitting)	3.463 x 10^1 (fitting)	1.224 x 10^{-8} (fitting)	6.663 x 10^5 (fitting)	4.123 x 10^{-10} (fitting)	8.220 x 10^2(fitting)	0.4
50^{0}C	1.000 x10^{-22} (Expt.)	5.352 x10^1 (Expt.)	2.860 x10^{-7}(Expt.)	1.000 x10^{15}(Expt.)	6.951 x10^{-9}(Expt.)	6.141 x10^4(Expt.)	
	1.000 x10^{-22} (fitting)	5.353 x10^1 (fitting)	2.859 x10^{-7}(fitting)	1.004 x10^{15}(fitting)	6.952 x10^{-9}(fitting)	6.141 x10^4(fitting)	3.47
100^{0}C	2.475 x10^{-6} (Expt.)	3.329 x10^1 (Expt.)	4.986 x10^{-8}(Expt.)	7.576 x10^3(Expt.)	1.661 x10^{11}(Expt.)	1.000 x10^{15}(expt.)	
	2.475 x10^{-6} (fitting)	3.329 x10^1 (fitting)	4.984 x10^{-8}(fitting)	7.575 x10^3(fitting)	1.647 x10^{11}(fitting)	1.001 x10^{15}(fitting)	0.42
150^{0}C	2.746 x10^{-6} (Expt.)	1.569 x10^1 (Expt.)	2.624 x10^{-7}(Expt.)	4.002 x10^2(Expt.)	8.460 x10^{-9}(Expt.)	7.658 x10^2(Expt.)	
	2.740 x10^{-6} (fitting)	1.597 x10^1 (fitting)	2.477 x 10^{-7}(fitting)	3.947 x10^2(fitting)	8.450 x10^{-9}(fitting)	7.704 x10^2(fitting)	2.21
200^{0}C	1.374 x10^{-5} (Expt.)	1.000 x10^{-2} (Expt.)	1.763 x10^{-8}(Expt.)	3.683 x10^4(Expt.)	9.519 x10^{-10}(Expt.)	5.526 x10^3(Expt.)	
	1.373 x10^{-6} (fitting)	8.594 x10^{-3} (fitting)	1.763 x10^{-8}(fitting)	3.682 x10^4(fitting)	9.518 x10^{-10}(fitting)	5.27 x10^3(fitting)	1.08
250^{0}C	1.229 x10^{-6} (Expt.)	1.000 x10^{-7} (Expt.)	1.461 x10^{-8}(Expt.)	8.111 x10^3(Expt.)	4.775 x10^{-10}(Expt.)	3.101 x10^3(Expt.)	
	1.229 x10^{-6} (fitting)	1.003 x10^{-7} (fitting)	1.461 x10^{-8}(fitting)	8.111 x10^3(fitting)	4.775 x10^{-10}(fitting)	3.101 x10^3(fitting)	1.90
300^{0}C	1.915 x10^{-6} (Expt.)	3.935 x10^1 (Expt.)	6.358 x10^{-8}(Expt.)	2.100 x10^2(Expt.)	7.893 x10^{-6}(Expt.)	7.830 x10^1(Expt.)	
	1.914 x10^{-6} (fitting)	3.937 x10^1 (fitting)	6.354 x10^{-8}(fitting)	2.100 x10^2(fitting)	7.890 x10^{-6}(fitting)	7.838 x10^0(fitting)	1.09
350^{0}C	3.208 x10^{-5} (Expt.)	1.000 x10^{-2} (Expt.)	2.048 x10^{-19}(Expt.)	1.000 x10^{-2}(Expt.)	2.558 x10^{-3}(Expt.)	4.628 x10^0(Expt.)	
	3.210 x10^{-5} (fitting)	1.079 x10^{-3} (fitting)	6.989 x10^{-14}(fitting)	7.555 x10^{-5}(fitting)	2.555 x10^{-7}(fitting)	4.635 x10^0(fitting)	8.97

AC conductivity analysis

Fig. 10(a) represents temperature and frequency response of ac conductivity of the $Bi_{0.6}La_{0.4}FeO_3$single perovskite. The formula used to calculate ac conductivity is $\sigma_{ac}= \omega\epsilon_r\epsilon_o\tan\delta$, where all the symbols have their usual meaning. The activation energy (E_a) of the sample can be calculated by using a mathematical relation; $\sigma_{ac} = \sigma_0 e^{-\frac{E_a}{K_B T}}$, where k_B = 1.38 x 10^{-23} J/K, E_a = activation energy and T = temperature. The slope of the curves in the **Fig. 10(a)** gives the value of the activation energies 677 meV, 389 meV, 317 meV and 201meV observed at different frequencies 10 kHz, 100 kHz, 1000 kHz and 5000 kHz respectively. This implies that activation energy increases with rise of temperature and help in the conduction mechanism because of the hopping of charge carriers [**51**] and demand the semiconductor nature of the sample. The movement of the oxygen vacancies may be related to this elevated activation energy at higher temperature [**52**]. **Fig. 10(b)** represents the variation of ac conductivity with frequency at different temperatures (25^{0}C to 350^{0}C). It is observed that at a fixed temperature, a low-frequency steady behavior of conductivity is called σ_{dc} and high-frequency dispersive conductivity is called σ_{ac}. At low frequency, ac conductivity increases with the rise of temperature supporting the thermally activated conduction process in the sample. As we move toward a higher frequency region, the value of ac conductivity increases slowly and suddenly attains peak value at a certain frequency is called hopping frequency, which is a temperature-dependent parameter.

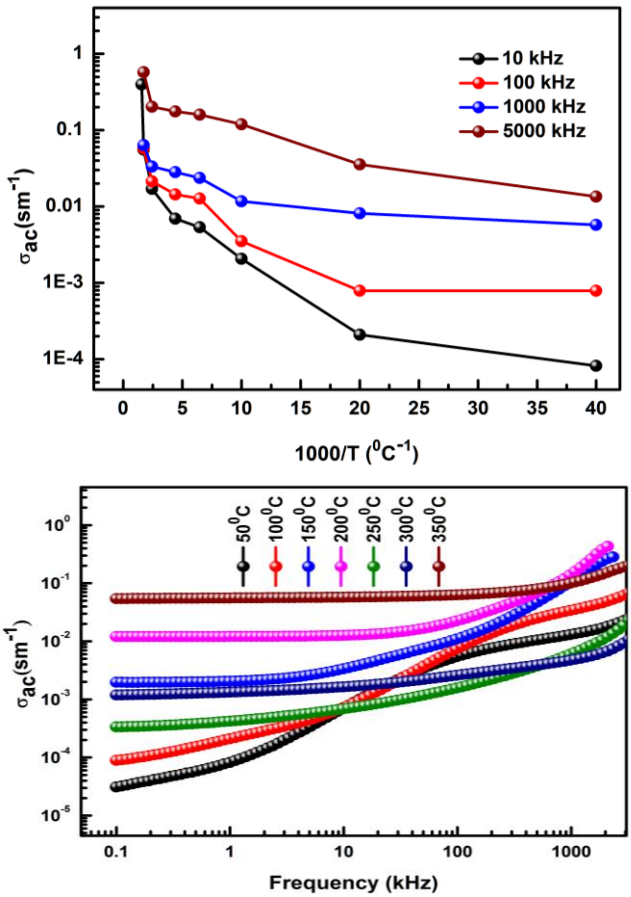

Fig. 10. (a) Temperature response curves of ac conductivity and (b) Frequency response curves of ac conductivity of the $Bi_{0.6}La_{0.4}FeO_3$ single perovskite.

Dielectric analysis

Fig. 11(a) shows dielectric constant (ε_r) and (**b**) tangent loss (*tan δ*) versus frequency of the $Bi_{0.6}La_{0.4}FeO_3$ single perovskite. It is observed that, the due to effect of grain boundaries the value of dielectric constant (ε_r) increases with rise of temperature. This character of the sample is root cause of different types of polarization, which may confirm ferroelectric nature in the studied [**53**]. This type of nature observed in the sample is found in good agreement with the proposed two layers model by Maxwell and Wagner [**54,55**]. The proposed model explains that the presence of dielectric properties in the prepared sample is due to the formation of two layers i.e., good conducting grains and poorly conducting grain boundaries.

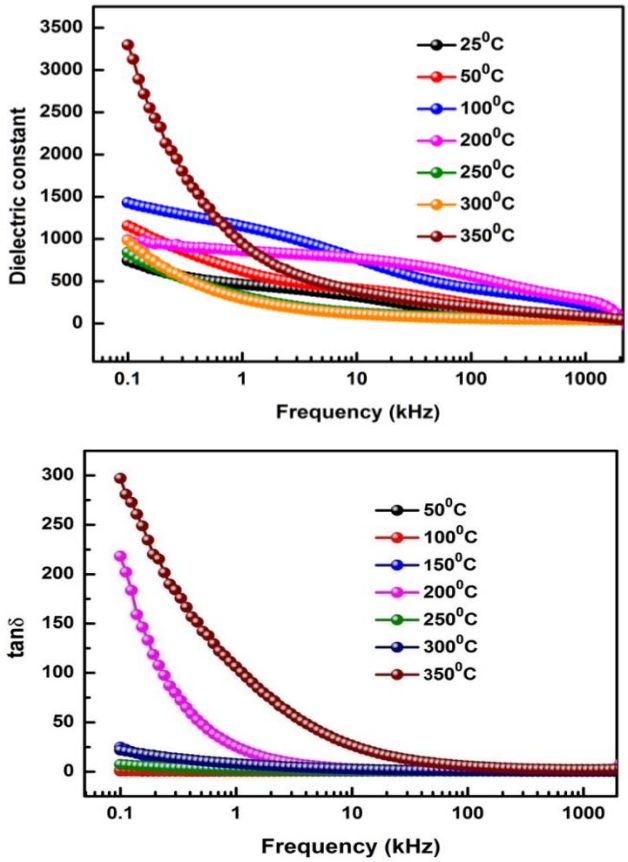

Fig. 11. (a) Frequency response curve of dielectric constant (b) Frequency response curve of tangent loss of the $Bi_{0.6}La_{0.4}FeO_3$ single perovskite.

The activity of the electrons at the grain boundaries increases in a low range of recorded frequency, whereas at grains it seems to be more active in the higher frequencies [**56**]. This indicates that grain boundaries are high resistance zone and require more energy to transfer the electric charges at low-frequency range so that both ε_r and tanδ have a higher value. But at a higher range of frequency, very small energy is required to electric charge carriers for overcoming the low resistance and resulting in a small dielectric loss.

Conclusion

$Bi_{0.6}La_{0.4}FeO_3$ single perovskite is prepared by convention high-temperature sintering technique. A phase transition occurs from rhombohedral (R3c) to orthorhombic (Pbnm) that confirmed by XRD analysis. The average crystalline size and lattice strain in the sample are about 63.8 nm and 0.147% respectively. The frequency bands corresponding to Bi-O, LaO, and FeO stretching vibration confirm that La^{+3} ions completely incorporate the Bi^{+3} ions in the A-site of the $BiFeO_3$perovskite. The SEM micrograph suggests that the sample has distinct grains and well-defined grain boundaries and the average grain size is about 13.9 μm. The activation energy increases from 201 meV to 677meV with temperature confirm that La modified bismuth ferrite undergoes a thermally activated conducting process. The thermally activated relaxation process is controlled by the immobile charge carriers in the host materials at low-temperature range while controlled by defects at higher temperatures which suggests hopping process play dominant role in the sample. The presence of asymmetrical curve of the electrical modulus plots suggests the non-Debye-type conductivity behavior. The presence of semi-circular arcs in the both Nyquist and Cole-Cole plots suggests the semiconductor nature of the sample.

Acknowledgement

The authors would like to extend their gratitude and sincere thanks to our host Institute for providing XRD and FTIR.

Conflict of Interest

The authors declare that there is no conflict of interest.

Keywords

Phase transition; lattice strain; ferrite perovskite; grain boundaries; perovskite; Nyquist plots

Received: 1 March 2021
Revised: 28 April 2021
Accepted: 29 May 2021

References

1. Michel, C.; Moreau, J.M.; Achenbach, G. D.; Gerson, R.; *Solid State Communications*, **1969**, *9*, 701.
2. V. Garcia, V.; Fusil, S.; Bouzehouane, K.S.; Mathur, N.D.; Barthelemy, A.; Bibes, M.; *Nature*, **2009**, *460*, 81.
3. Eerenstein, W.; Mathur, N.D.; Scott, J.F.; *Nature*, **2006**, *442*, 759.
4. Kumar, A.; Yadav, K.L.; **2011**, *176*, 227.
5. Yang, J.C.; He, Q.; Yu, P.; Chu, Y.H.; *Ann. Rev. Mater. Res.*, **2015**, *45*, 249.
6. Wang, Nan; Luo, Xudong; Han, Lu; Zhang, Zhiqiang; Zhang, Renyun; Olin, Håkan; Yang, Ya; *Nano-Micro Lett.;* **2020**, *81*, 1.
7. Qi, J.; Ma, N.; Ma, X.C.; Adelung, R.; Yang, Y.; *ACS Appl. Mater. Interfaces*, **2018**, *10*, 13712.
8. Dzyaloshinskii, I.E.; *Sov. Phys.-JETP*, **1959**, *10*, 628.
9. Astrov, D.N.; *Sov. Phys.-JETP*, **1960**, *11*, 708.
10. O'Dell, T.H.; The Electrodynamics of Magneto-Electric Media (Amsterdam: North-Holland), **1970**.
11. Kubel, F.; Schmid, H.; *Acta Crystallographica, Section B, Structure Science*, **1990**, *46*, 698.
12. Gustau, C.; Scott, J.F.; *Adv. Mater.*, **2009**, *21*, 2463.
13. Velev, J.P.; Jaiwal, S.S.; Tsymbal, E.Y.; *Phil. Trans. R. Soc. A*, **2011**, *369*, 3069.

14. Chunlin Fu; Long, X.; Cai, W.; Chen, G.; Deng, X.; *Ferroelectric*, **2014**, *460*, 157.
15. Wang, J.; Neaton, J.B.; Zheng, H.; Nagarajan, V.; Ogale, S.B.; Liu, B.; Viehland, D.; Vaithyanathan, V.; Schlom, D.G.; Waghmare, U.V.; Spaldin, N.A.; Rabe, K.M.; Wuttig, M.; Ramesh, R.; *Science*, **2003**, *299*, 1719.
16. Soram, B.S.; Ngangom, B.S.; Sharma, H.B.; *J. Thin Films*, **2012**, *524*, 57.
17. Uniyal, P.; Yadav, K.L.; *Journal of Physics-Condensed Matter*, **2009**, *21*, 405901.
18. Hemanta Singh, H.; Churchill Singh, E.; Basantkumar Sharma, H.; *Integrated Ferroelectrics*, **2019**, *203*, 108.
19. Voorhoeve, R. J. H.; Advanced materials in catalysis, Acad. Press, **1977**.
20. Robert Ian Hines. Atomistic simulation and ab-initio studies of polar solids. Phd, Bristol, **1997**.
21. Shannon, R.D.; *Acta Crystallographica*, **1976**, *A32*, 751.
22. Parida, R.K.; Pattanayak, D.K.; Parida, B.N.; *J. Mater. Sci. Mater. Electron*, **2017**, *28*, 16689.
23. Parida, S.K.; Choudhary, R.N.P.; Achary, P.G.R; *Int. J. Microstructure and Materials Properties*, **2020**, *15*, 107.
24. Parida, B.N.; Parida, R.K.; Panda, A.; *J. Alloys Comp.*, **2017**, *696*, 338.
25. Ebrahim, S.; Ghahfarokhi, S.E.M.; Larki, M.R.; Iraj, K.; *IEEE Transition on Magnetics*, **2020**, *52*, 2000109.
26. Silva, J.; Reyes, A.; Esparza, H.; Camacho H.; Fuentes, L.; *Integrated Ferroelectrics*, **2011**, *126*, 47.
27. Moreau, J. M.; Michel, C.; Gerson, R.; James, W.J.; *J. Phys. Chem. Solids*, **1971**, *32*, 1315.
28. Kubel, F.; Schmid, H.; *Acta Cryst. B.*, **1990**, *46*, 698.
29. Cullity B.D.; Stock, R.S.; Elements of X-Ray Diffraction, Prentice Hall, New Jersey, 3rd Edn, **2001**
30. Parida, S.K.; Mohapatra, Jyoshnarani; Mishra, D.K.; *Materials Letters*, **2016**, *181*, 116.
31. Parida, S.K., *Advanced Science Letters*, **2016**, *22*, 584.
32. Hang, Q.; Xing, Z.; Zhu, X.; Yu, M.; Song, Y.; Zhu, J.; Liu, Z.; *Ceram. Int.*, **2012**, *38*, S411.
33. Ghoneim, N.A.; Batal, H.A.EI; Abdel Shafi, N.; Azooz, M.H.; Proceeding of the Egyptian Conference of Chemistry, Cairo, **1996**, Vol.162.
34. JaziaKharrat, A. Ben; Moutiab, N.; Khirouni, K.; Boujelben W.; *Materials Research Bulletin*, **2018**, *105*, 75.
35. Padmasree, K.P.; Kanchan, D.K.; Kulkami, A.R.; *Solid State Ionics*, **2006**, *177*, 475.
36. Chowdari, B.V.R.; Gopalkrishnnan, R.; *Solid State Ionics*, **1987**, *23* 225.
37. Barik, S.K.; Mahapatra, P.K.; Choudhary, R.N.P.; *Appl. Phys A*, **2006**, *85*, 199.
38. Hou, Zhi-Ling; Cao, Mao-Sheng; Yuan, Jie; Fang, Xiao-Yong; Shi, Xiao-Ling; *J. Appl. Phys.*, **2009**, *105*, 076103.
39. Sinha, S.K.; Choudhary, S.N.; Choudhary, R.N.P.; *J. Mater. Sci.*, **2004**, *39*, 315.
40. Hajra, S.; Sahu, M.; Purohit, V.; Choudhary, R.N.P.; *Heliyon*, **2019**, *5*, 01654.
41. Dehury, S.K.; Achary, P.G.R.; Choudhary, R.N.P.; *J. Mater. Sci. Mater. Electron.*, **2018**, *29*, 3682.
42. Selvasekarapandian, S.; Vijaykumar, M.; *Mater. Chem. Phys.*, **2003**, *80*, 29.
43. Hossen, M.B.; Hossain, A.K.M.A.; *J. Adv. Ceram.*, **2015**, *4*, 225.
44. Jonscher, A.K.; *Nature*, **1977**, *267*, 673.
45. Ke, Q.; Lou, X.; Wang, Y.; Wang, J.; *Phys. Rev. B Condens. Matter Mater. Phys.*, **2010**, *82*, 024102.
46. Thakura, S.; Raia, R.; Bdikinb, I.; Almeida Valente, M.; *Mater. Res.*, **2016**, *19*, 1.
47. Khlifi, A.; Hanen, R.; Mleiki, A.; Rahmouni, H.; Guermazi, N.; Khirouni, K.; Cheikhrouhou, A.; *Eur. Phys. J. Plus*, **2020**, *135*, 790.
48. Sen, S.; Choudhary, R. N. P.; Pramanik, P.; *Phys. B Condens. Matter*, **2007**, *387*, 56.
49. Belboukhari, A.; Choukri, E.; Gagou, Y.; Elmoznine, R.; Abdelmoula, N.; Neqali, A.; Marssi, M., EI; Khemakhem, H.; Mezzane, D.; *Superlattices Microstruct*, **2014**, *71*, 1145.
50. Parida S.K.; Choudhary, R.N.P.; Achary, P.G.R.; *Ferroelectrics*, **2019**, *551*, 109.
51. Lj. Kundakovic Li; Flytzani-Stephanopoulos, M.; *Journal of Catalysis*, **1998**, *179*, 203.
52. Arandiyan, H.; Dai, H.; Ji, K.; Sun, H.; Li, J.; *ACS Catal.*, **2015**, *5*, 1781.
53. Rezlescu, N.; Rezlescu, E.; Popa, P.D.; Doroftei, C.; Ignat, M.; *Ceram. Int.*, **2015**, *41*, 4430.
54. Alexander, L.; Klug, H.P.; *J. Appl. Phys.*, **1950**, *21*, 137.
55. Pawar R. P.; Puri, V.; *Ceram. Int.*, **2014**, *40*, 10423.
56. Milt, V. G.; Spretz, R.; Ulla, M.A.; Lombardo, E.A.; García Fierro, J.L.; *Catalysis Letters*, **1996**, *42*, 57.